

EXPERIMENTAL STUDIES OF MILLIMETER-WAVE SCATTERING IN DISCRETE RANDOM MEDIA AND FROM ROUGH SURFACES

Y. Kuga and P. Phu

- 1. Introduction**
- 2. Random Media for Controlled Experiments**
 - 2.1 Introduction
 - 2.2 One-Dimensional Rough Surfaces
 - 2.3 Two-Dimensional Rough Surfaces
 - 2.4 Computer-Aided Manufacturing of Rough Surfaces
 - 2.5 Random Discrete Media for Microwave and MMW Experiments
 - 2.6 Random Media for Optical Experiments
- 3. Experimental Systems**
 - 3.1 Introduction
 - 3.2 VNWA as an Microwave and MMW Receiver
 - 3.3 MMW Systems
 - 3.4 Calibration of the MMW Systems
- 4. Experimental Results on Rough Surfaces and Discrete Random Media**
 - 4.1 Introduction
 - 4.2 Effects of the Surface Correlation Functions on the MMW Scattering Characteristics
 - 4.3 MMW Scattering from 2-Dimensional Rough Surfaces
 - 4.4 Velocity of Coherent and Incoherent Electromagnetic Waves in Dense Strongly Scattering Media

5. Conclusions

References

1. Introduction

In recent years, there has been a surge of interest in the multiple scattering of waves in random media, particularly in connection with enhanced backscattering and localization also known as *Anderson localization* [2–4,46,52]. The backscattering enhancement phenomenon is a direct consequence of the coherent interference of multiple scattered waves which add constructively in the back direction. The existence of enhancement was originally predicted for a wave scattered from turbulence [5]. Its existence, however, was discovered in the controlled experiments conducted with latex microspheres at optical wavelengths [6–7]. A very narrow enhanced peak in the back direction was observed for a certain range of size parameters and fractional volume densities. This phenomenon was subsequently explained as the constructive interference in the multiple scattering using the second-order multiple scattering theory [9]. Physicists working in solid state physics realized that the backscattering enhancement is essentially the same as the electron localization effect predicted by Anderson in 1958. Under certain conditions the electromagnetic wave can be strongly localized due to multiple scattering, and the diffusion constant that is related to the propagation of the incoherent wave becomes very small. This phenomena is known as *strong localization*.

Many naturally occurring phenomena, such as the high reflectivity of the moon at full moon and the glory appearing around the shadow of an airplane on a cloud when viewed from the airplane, may be related to the backscattering enhancement [10]. Likewise, scientists conducting remote sensing research on geophysical media may have observed backscattering enhancement but could not distinguish it from ordinary scattering phenomena. The difficulty of knowing the accurate characteristics of random media has been the major problem if the experiment is conducted *in situ*.

During the past decade, extensive research on wave scattering from rough surfaces has been conducted. Early experimental research on rough surface scattering was limited to measuring the scattering from natural or poorly characterized surfaces [12]. The pioneering experiments, in which the strong backscattering enhancement was observed, were conducted with carefully fabricated very rough surfaces of known characteristics at optical wavelengths [13–14]. The findings spurred a surge of research on numerical, theoretical and experimental

studies on wave scattering from rough surfaces [15–19,52]. Once again the importance of controlled experiments was demonstrated. We will discuss the experimental techniques used for studying millimeter-wave scattering from rough surfaces and discrete random media. A detailed description of the surface fabrication method and the experimental system will be presented.

2. Random Media for Controlled Experiments

2.1 Introduction

In controlled experiments, the detailed characteristics of the random medium must be known in order to compare the results with a theory or numerical simulations. For example, to conduct experimental studies on wave scattering from random rough surfaces, we must be able to either measure the surface profile so that surface statistics can be obtained or create a surface of known statistical properties. In addition, the material characteristics, such as conductivity and dielectric constant, must be known at the measured wavelength. Similarly, experiments involving discrete random media require information on particle-size distributions, particle shapes, particle locations, and material characteristics. Since the scattering is usually dominated by targets whose dimensions are comparable to or greater than the wavelength, the relative dimension with respect to the wavelength is an important parameter for characterizing the random media. The accuracy of the size distributions and surface profiles must be specified in terms of wavelength rather than the absolute scale. A difference of one μm in surface profile is too large for an optical experiment, but the effect is negligible for a MMW experiment.

In the following section, we will describe the rough surface and discrete random fabrication methods which are used for our MMW experiments. A detailed description of 1- and 2-dimensional surface generation and fabrication will be presented in Section 2.2, 2.3, and 2.4. Optical experiments with lasers and random media of known characteristics have been studied extensively in the past. Therefore, only a brief discussion of random media for optical experiments is given in Section 2.6.

2.2 One-Dimensional Rough Surfaces

In most research on rough surfaces, the rough surface is described in terms of its deviation from a smooth “reference plane”. In general, the reference plane is assumed to be located at $z = 0$. The random fluctuations from this reference plane are denoted by the function $z = f(x)$. For 1-D rough surfaces, two parameters are used to describe the statistical properties. They are the rms height h and the correlation length l . The probability density function of the surface height $P(z)$ introduces the element of randomness in the surface and describes the one-point statistics of the rough surface. For analytical convenience, most of the research on rough surfaces assumes that the surface height distributions are Gaussian, i.e.,

$$P(z) = \frac{1}{h\sqrt{2\pi}} \exp\left(-\frac{z^2}{2h^2}\right) \quad (1)$$

There are many questions concerning the validity of using such Gaussian distributions to represent natural rough surfaces. In practice, many rough surfaces formed by natural processes or engineering methods are not entirely Gaussian [41], and the use of the Gaussian process is justified only for ease of numerical and analytical modeling. For rough surfaces formed by stationary stochastic processes, the correlation function of the surface $C(\tau)$ describes the two-point statistics of the surface.

$$C(\tau) = \frac{\langle f(x)f(x+\tau) \rangle}{h^2} \quad (2)$$

$C(\tau)$ describes the spatial coherence between different points on the surface separated by a distance τ . Several correlation functions can be found in the literature. The most widely used correlation function is the Gaussian correlation,

$$C(\tau) = h^2 \exp\left(-\frac{\tau^2}{l^2}\right) \quad (3)$$

The correlation length l is statistically equivalent to the average “period” of the rough surface. Surfaces with a large correlation length have peaks separated by a large distance on average and surfaces with a small correlation length have tightly separated peaks. An alternative correlation function which more accurately describes surfaces with very sharp peaks is the exponential function. This has the form

$$C(\tau) = h^2 \exp\left(-\frac{|\tau|}{l}\right) \quad (4)$$

Many other forms of surface correlation functions can be used to model surfaces formed by different processes. They include the Lorentzian and the Gaussian cosine autocorrelation functions.

The power spectral density function of the surface $W(k)$, also known as the surface spectrum, is related to the correlation function by a one-dimensional Fourier transform. Physically, k represents the spatial frequency and it has the units of m^{-1} . $W(k)$ is the average distribution of each spatial frequency component of the randomly fluctuated surface profile. Surfaces with rapid variations and sharp edges have a non-zero spectrum value at large spatial frequency components. For a Gaussian correlation, the corresponding spectral density is the Fourier transform of Eq. (3) and is given by

$$W(k) = \frac{h^2 l}{\sqrt{4\pi}} \exp\left(-\frac{k^2 l^2}{4}\right) = \frac{1}{2\pi} \int_{-\infty}^{\infty} C(\tau) e^{ik\tau} d\tau \quad (5)$$

The power spectrum of an exponential correlation function is the Fourier transform of Eq. (4) and is given by

$$W(k) = \frac{h^2 l}{\sqrt{4\pi}} \left(\frac{1}{1 + k^2 l^2} \right) \quad (6)$$

In turbulence modeling, the power law spectrum is used to model the random fluctuations of the propagation characteristics of the medium. Its corresponding spectrum is given by

$$W(k) = \frac{h^2 l}{\sqrt{4\pi}} \left\{ 1 + \pi \left[\frac{(2n-3)!!}{(2n-2)!!} \right]^2 \frac{k^2 l^2}{4} \right\}^{-n} \quad (7)$$

$$(2n-2)!! = 2 \times 4 \times \cdots \times (2n-2)$$

$$(2n-3)!! = 1 \times 3 \times \cdots \times (2n-3)$$

$$(-1)!! = 1$$

where n is the order of the power law spectrum. The power law spectrum converges to a Gaussian spectrum for large order n , and is almost equivalent to the Laurentzian spectrum for $n = 1$ order. Moreover, for any given order, the power law spectrum reduces to k^{-2n} for large k . No closed form solution is available for the autocorrelation of a surface with a power law spectrum. We only consider the Gaussian and power law spectrums since the fabrication for surfaces with an exponential spectrum is very difficult due to limited physical tolerance. In Figure 2.1, the spectral distributions of the three different types of surface spectrums are shown for the case of a rough surface with $h = 1\lambda$ and $l = 3\lambda$. The roughness spectrum of the surface is shown for surfaces with Gaussian, power law ($n = 2$) and exponential surface correlation functions. From the figure, it is clear that the exponential spectrum has a heavy tail which results in surfaces with a very rapidly varying small-scale roughness superimposed on the Gaussian roughness. The power law $n = 2$ case lies in-between the exponential and Gaussian cases. In Figure 2.2, comparisons of the corresponding surface profiles are shown. The surface profile with a Gaussian spectrum is shown in both parts. In Figure 2.2(a) another surface with a power law spectrum $n = 2$ is superimposed onto the surface with a Gaussian spectrum; and in Figure 2.2(b), another surface with an exponential spectrum is shown. The surface roughness characteristics are $h = 1\lambda$ and $l = 3\lambda$, and the surface length is $L = 30\lambda$. The small-scale roughness arising from the high frequency tail of both the second-order power law spectrum and the exponential spectrum is evident in the picture. It will be shown later that the local small-scale roughness affects the scattering characteristics in an important way.

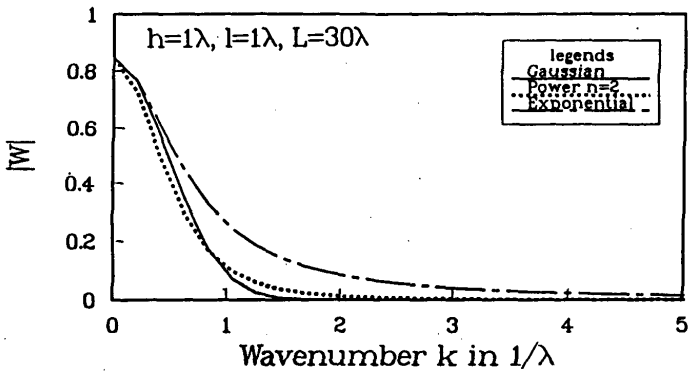


Figure 2-1. Comparison of three different surface spectral densities. $h = 1\lambda$ and $l = 3\lambda$.

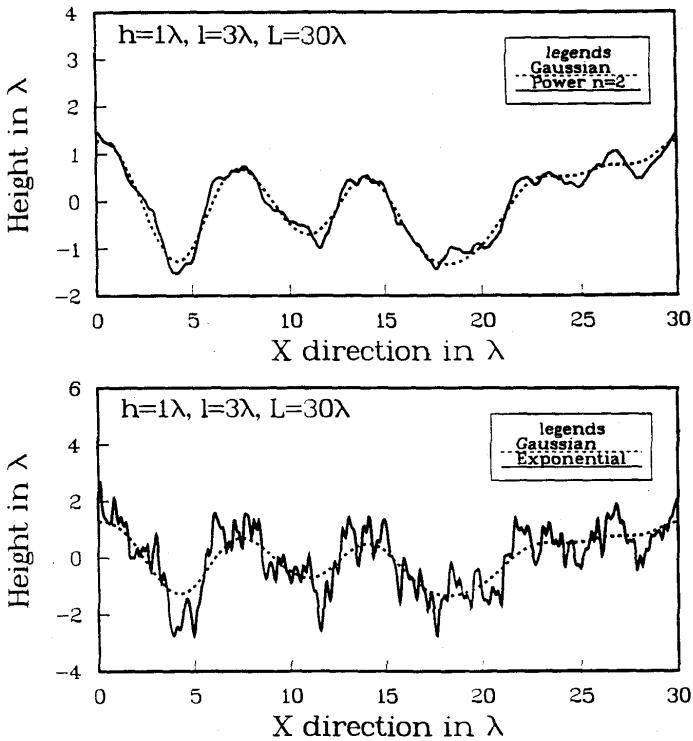


Figure 2-2. Comparison of surfaces with different spectral densities. (a) Type I (Gaussian) and Type II (power law, $n = 2$), (b) Type I (Gaussian) and Type III (exponential).

To generate a rough surface numerically, a sequence of normally distributed random numbers are used in the phase of the surface spectrum [20]. Using the discrete Fourier transform method (DFT), the rough surface profile $z = f(x_n)$ is related to the 1-D DFT of the surface spectrum as follows:

$$f(x) = \frac{1}{L} \sum_{n=-\frac{N}{2}}^{\frac{N}{2}-1} F(K_n) \exp(iK_n x) \quad (8)$$

where

$$F(K_n) = \sqrt{2\pi LW(K_n)} \left\{ \begin{array}{l} \frac{N(0,1) + iN(0,1)}{\sqrt{2}}, n \neq 0, \frac{N}{2} \\ N(0,1), n = 0, \frac{N}{2} \end{array} \right\} \quad (9)$$

$$K_n = \frac{2\pi n}{L}, \quad i = \sqrt{-1}$$

$N[0,1]$ denotes a sequence of normally distributed numbers in $[0,1]$ with zero mean and unity standard deviation. In the above equation, the one-point statistics are governed by the random modulation in the phase of the Fourier coefficients. For a *p.d.f.* of height with another distribution such as Gamma distribution, it suffices to replace $N[0,1]$ by an appropriate distribution. The two-point statistics are governed by the magnitude of the Fourier spectrum which follows the surface spectrum $W(k)$. Since the surface must be represented by a sequence of real numbers, the phase of the Fourier coefficients must satisfy certain requirements. In order to generate a real sequence, the Fourier coefficients of the function $F(K_n)$ must satisfy the following condition

$$F(K_n) = F^*(-K_n) \quad (10)$$

The above requirement is very important in the surface synthesis for the 2-D case. The use of DFT in the rough surface implementation requires that the surface lengths be at least five correlation lengths so that no spectral aliasing is presented in the resulting surface [21]. Furthermore, the resulting rough surface is a periodic function in which the surface height, and the first- and second-order slopes are periodic in space. It is important to note that due to a finite surface length

in the discrete synthesis process, the surface autocorrelation does not completely decay to zero and some oscillations are presented. If the inverse Fourier transform of the actual correlation is performed in order to obtain the power spectrum, a windowing function such as a *Hanning* window must be applied to the original sequence in order to avoid aliasing and edge effects [21]. In practice, the surface spectrum can be estimated from the actual surface profile by the following equation

$$W(k) = \frac{1}{2\pi L} \left\langle \left| \int_{-L/2}^{L/2} g(x) f(x) e^{-ikx} dx \right|^2 \right\rangle \quad (11)$$

The windowing function $g(x)$ with an appropriate tapering is to minimize spectral sidelobe, also known as the ‘‘Gibbs phenomena’’ in Fourier series analysis, due to the finite surface length.

2.3 Two-Dimensional Rough Surfaces

Most of the statistics used to describe 1-D rough surfaces can be extended to the 2-D case. The 2-D rough surface is described by $z = f(x, y)$, which is a random function of position (x, y) . Various two-dimensional spectra and autocorrelations, which are basically extensions of the one-dimensional case, can be described. However, the manufacturing of 2-D rough surfaces is much more difficult and time consuming than that of the 1-D case. The presence of higher frequency variations in the 2-D surface profiles demands very strict physical tolerances during the manufacturing process. Therefore, for reasons of practicality in surface manufacturing, only surfaces with Gaussian roughness and Gaussian spectrum are considered. The correlation function $C(\tau_x, \tau_y)$ which describes the coherence between different points on the surface separated by the distance $d = \sqrt{\tau_x^2 + \tau_y^2}$, is given by

$$C(\tau_x, \tau_y) = h^2 \exp \left(-\frac{\tau_x^2}{2l_x^2} - \frac{\tau_y^2}{2l_y^2} \right) \quad (12)$$

τ_x and τ_y describe the separation between any two points along the x and y directions. The coherence length of the surface profiles is given by l_x and l_y . The power spectral density function of the surface $W(k_x, k_y)$ is related to the correlation function via a two-dimensional

Fourier transform. For a Gaussian correlation function,

$$W(k_x, k_y) = \frac{l_x l_y h^2}{4\pi} \exp\left(-\frac{k_x^2 l_x^2}{4} - \frac{k_y^2 l_y^2}{4}\right) \quad (13)$$

It is important to note that in Eq. (13), there are two distinct correlation lengths, l_x and l_y . The surface is isotropic if $l_x = l_y$, and anisotropic if $l_x \neq l_y$. On the other extreme, if one of the correlation lengths is much larger than the other, the 2-D surface is essentially a one-dimensional surface for the purpose of the experiments and the numerical calculations. Similar to the 1-D case, the rough surface profile $z = f(x, y)$ is related to the 2-D DFT of the power spectrum as follows,

$$f(x, y) = \frac{1}{L^2} \sum_{m=-\frac{N}{2}}^{\frac{N}{2}-1} \sum_{n=-\frac{N}{2}}^{\frac{N}{2}-1} F(K_{xm}, K_{yn}) \exp(iK_{xm}x + iK_{yn}y) \quad (14)$$

where

$$F(K_{xm}, K_{yn}) = 2\pi L \sqrt{W(K_{xm}, K_{yn})} \begin{cases} \frac{N(0,1)+iN(0,1)}{\sqrt{2}}, & m, n \neq 0, \frac{N}{2} \\ N(0, 1) & m, \text{ or } n = 0, \frac{N}{2} \end{cases} \quad (15)$$

$$K_{xm} = \frac{2\pi m}{L}, \quad K_{yn} = \frac{2\pi n}{L} \quad i = \sqrt{-1}$$

K_{xm} and K_{yn} are the discrete set of spatial frequencies. To generate a real sequence, the requirement for $F(K_{xm}, K_{yn})$ is as follows

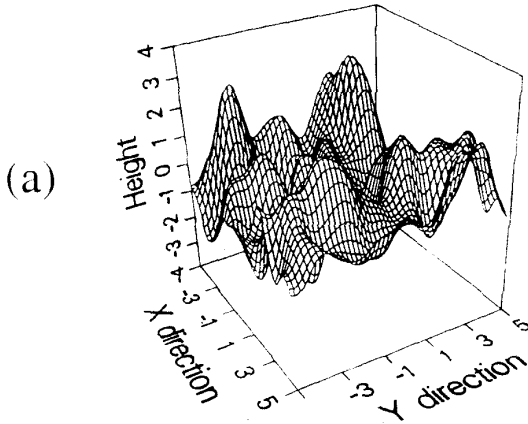
$$F(K_{xm}, K_{yn}) = F^*(-K_{xm}, -K_{yn})$$

and

$$F(K_{xm}, -K_{yn}) = F^*(-K_{xm}, K_{yn})$$

Under the above two conditions, the 2-D sequence is ‘‘conjugate symmetrical’’ about the origin. This means that the reflection of any point about the origin is its complex conjugate. Figure 2.3 shows typical 2-D surface profiles generated numerically. Part (a) has a surface roughness $h = 1, l_x = 1$ and $l_y = 1$, and part (b) has an anisotropic surface with $h = 1, l_x = 1$ and $l_y = 3$.

Isotropic surface $h=\lambda$. $l_x=l_y=\lambda$



Anisotropic surface $h=0.5\lambda$. $l_x=2\lambda$. $l_y=0.5\lambda$

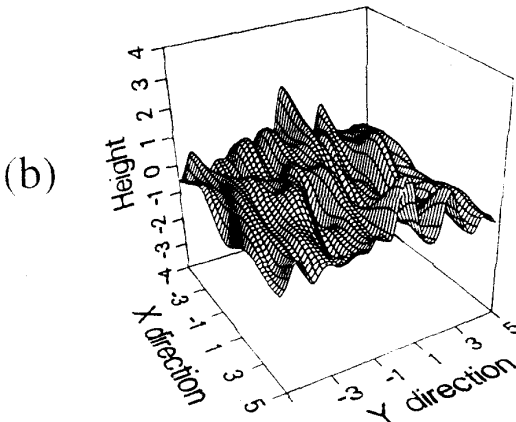


Figure 2-3. Two-dimensional rough surface profile generated numerically.

Figure 2-4. 1-D rough surface: actual trace of toolpath for automatic machining of rough surface superimposed by the actual numerical profile.

2.4. Computer-Aided Manufacturing of Rough Surfaces

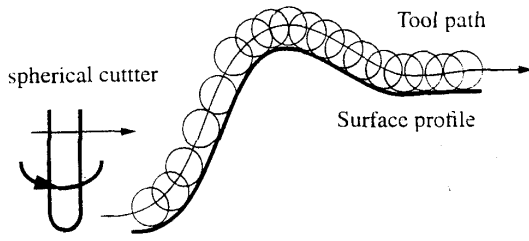
Both 1-D and 2-D rough surfaces are created on the computer using the spectral method outlined in the previous two sections. The surfaces are translated into an equivalent machine representation appropriate for the digital controller of the CNC milling machine. The software is based on an industry standard computer-aided-design (CAD) milling program (Mastercam) distributed by Techno. In the case of a 1-D rough surface, the 1-D profile of each surface is read into the MasterCam software for processing. Cutting paths orthogonal to the profile are then generated numerically considering the size of the cutting tool and the step size of the cutting path. The resulting tool path is displayed interactively on the computer screen to verify the accuracy of the cutting process. Figure 2-4 shows a typical 1-D rough surface together with the path traversed by the tool. As seen from the figure, very little cutting error exists for the 1-D case and the accuracy of the software is established. One-dimensional surfaces with different types of roughness are manufactured for Gaussian and power law spectra for the experiments. The experimental results for these surfaces are presented in a subsequent section.

In the case of a 2-D rough surface, the complexity and the processing time required for the corresponding 3-D toolpath generation sequence is several orders of magnitude greater than the 1-D case. A two-dimensional lattice representing the rough surface is processed by an Intel 486 based computer. Before the three-dimensional surface describing the toolpath can be computed, a parametric tensor spline representation known as the COONS surface is needed to represent the surface [22–23]. The tensor representation results in a large banded matrix which contains the coefficients required to determine the local directional derivatives at each point of the surface. In order to determine the location of the tip of the cutting tool correctly, the spherical radius of the tool, the tangential and normal directional derivatives, and the local radius of curvature of the surface must be considered. The resulting tool path describes a 3-D surface which is offset from the original surface. It is important to point out that the offset distance is a function of the location of the cutting tool relative to the surface. During the cutting process, the center of the tool does not travel in a straight line along the direction of cutting but rather makes small detours along the curvature of the surface.

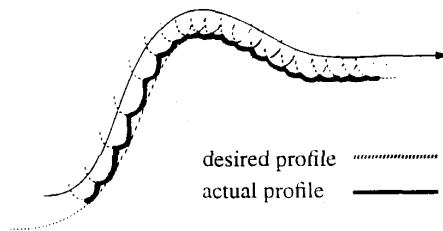
The processing requires an iterative matrix inversion to obtain all the spline coefficients. The details of the numerical control algorithm is very complex [23] and are not included. Consequently, the dimensions of each type of surface are chosen for optimum processing time and acceptable accuracy. There are several factors that must be considered in order to obtain a successful surface tool path. The first factor that affects the surface processing is the surface resolution. In order to obtain an unique solution to the spline coefficients everywhere on the surface, there is a minimum requirement on the number of points per millimeter. For example, the smaller the correlation length of the surface, the more points must be used to represent the surfaces accurately. Failing to do so usually results in divergent solutions to the surface spline coefficients because the local directional derivatives are too large. For example, for a given surface with a correlation length l and rms height h , the average rms slope is $\sqrt{2}h/l$. However, as the surface height is normally distributed, the chance of having the magnitude of a local derivative lying between the range of $[\sqrt{2}h/l, 2\sqrt{2}h/l]$ is about 27% and that between the range of $[2\sqrt{2}h/l, 3\sqrt{2}h/l]$ is about 5%. This means that an ample number of points for discretizing the surface using a reasonably high resolution must be provided. In general, for a given surface, several small samples with different surface resolutions are processed before the final surface is committed for manufacturing. The second factor that affects the processing is the dimensions of the surface. Since the processing requires matrix solutions, the processing time is of the order of $O(N_s^\alpha)$, where N_s is the total number of lattice points representing the surface. In order to keep the required processing time to an optimum value, the overall size of the surface and the surface resolution are set accordingly.

After the 2-D tool path for creating each surface is generated, the rough surface is machined using an CAM milling machine. The control program for the milling machine is provided by Techno which serves as the post processor of the MASTER CAM software. The accuracy of the milling process is directly related to the size of the cutting tool. In order to obtain a highly accurate surface profile, small ball-end mills with a 2 mm diameter are used. In order to ensure that the final surface is free of grating effects known as “scallops”, a distance of 0.5 mm between adjacent cutting passes is used. It is quite obvious that the size of the scallops is directly proportional to the distance between the tool pass and the actual slope of the surface, as shown in Figure 2.5.

This observation is especially important for the case of a 2-D rough surface since the tool can only cut vertically at the fixed horizontal point. In the 2-D case, the actual 2-D tool paths are displayed on the computer screen and are visually inspected for good accuracy. Since the software is a mini version of an industrial CAM milling machine used to produce high precision parts, the accuracy of the machine is guaranteed by the manufacturer. The CNC milling machine and the corresponding 2-D rough surface made during the machining process are shown in Figure 2.6. In Figure 2.6(a), the CNC milling machine with the (x, y, z) translational stages is shown, with samples of 1-D and 2-D surfaces. In Figure 2.6(b), the 2-D surface profile together with the 2-D cutting toolpath are shown. The two vertical lines on the left bottom corner of the figure depict the entrance and the exit trace of the cutting tool. The three-dimensional toolpath which is depicted by the offset surface depends on the physical dimensions of the cutting tool used.

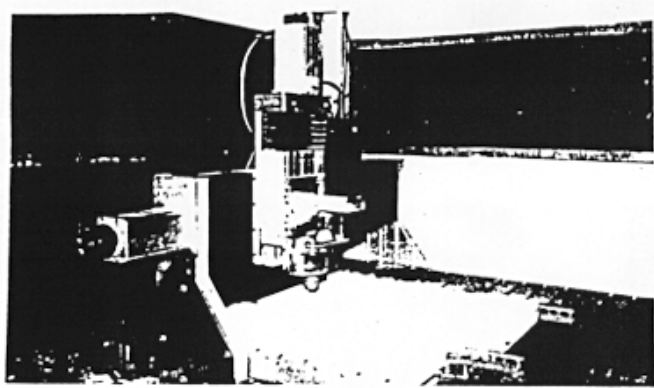


(a) Example of the tool path of a spherical tool

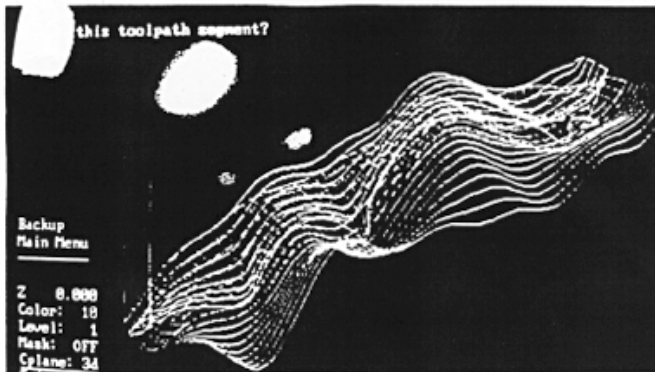


(b) Resulting machined surface with $d/2$ resolution

Figure 2-5. Scallop formed by a cutting tool of diameter d . The cutting pass is $d/2$ in order to exaggerate the extent of the scallops.



(a) CNC milling machine



(b) CAD/CAM manufacturing

Figure 2-6. Computer Aided Manufacturing (CAM) of 2-D rough surfaces using a computer-numerical-controlled (CNC) milling machine. (a) CNC milling machine with x-y-z translational stage. (b) CAD/CAM software for determining the three-dimensional tool path for a given 2-D surface profile.

Figure 2-7. 2-D pair distribution function - Experiment and theory: 10.9% fractional volume density. Dashed curve is computed result using Percus-Yevick approximation. Solid curve is experimental result using the known particle positions.

2.5 Random Discrete Media for Microwave and MMW Experiments

In general, the particle size of the discrete random media for microwave and MMW experiments is greater than several millimeters, and water or other liquids cannot be used for suspending particles due to high absorption. Beard et al. used styrofoam particles suspended by air blown from the bottom of the container [11]. With this method, a high concentration of particles as well as random distributions can be obtained. However, light materials such as styrofoam have a dielectric constant of only 1.05 at the microwave frequency. Another approach is the fabrication of random media by embedding particles into a thin layer of soft materials [24–28]. To embed particles, holes with a slightly smaller diameter than that of the particle are machined at positions generated by a random number generator. The use of a computer controlled milling machine with a CAD system significantly improves the accuracy and reduces the fabrication time. Because the media are stationary and the position of particles are generated by a computer, the statistical data including the pair-correlation function can be readily obtained [25]. Figure 2-7 shows an example of a pair-correlation

function in a 2D transverse plane of 6 mm glass particles embedded in layers of styrofoam. Statistically independent samples are created by shuffling layers. To maintain the mechanical strength, the number of holes that can be machined in each layer must be limited. A densely distributed non-tenuous two-dimensional structure is also fabricated with glass rods and a CAD/CAM system [28].

2.6 Random Media for Optical Experiments

In the optical experiments, the wavelength of the incident wave is usually limited by the availability of lasers such as Argon ($0.488 \mu\text{m}$), HeNe (0.633 and $1.152 \mu\text{m}$), and Nd YAG ($1.06 \mu\text{m}$). If the random media must be characterized within 10% of the wavelength, the required accuracy will be less than $0.1 \mu\text{m}$. Because of this, the rough surface fabrication technique at the optical wavelength is totally different from that of the MMW regime. Researchers at the Imperial College developed a rough surface fabrication method using the photoresist and speckle exposure technique [13–14]. With this method, a sample surface was prepared by coating thin layers of photoresist on a glass substrate. Then the surface is exposed to a number of speckle patterns created by an Argon Ion or HeCd laser. Finally, the plate is processed in a photoresist developer to produce a linear relation between exposure time and surface height. The exposure time and the intensity of the laser light determine the etching depth. In general, the statistics of a single speckle intensity pattern are given by a Rayleigh distribution. By exposing a surface to many statistically independent speckle patterns with equal exposure time, the height distribution close to the Gaussian is obtained [14]. The correlation function of the surface is determined by that of the exposing speckle pattern. To make a good reflecting surface, the sample is usually coated with gold. Both one and two-dimensional surfaces have been fabricated with this technique.

Unlike the surface machining technique discussed in Section 2.3, the rough surfaces fabricated with the speckle exposure technique must be measured to find an rms height and correlation length [14]. In general, characterizing the very rough surfaces at an optical wavelength is a challenging task to say the least. A stylus-based profilometer is effective for smooth to moderately rough surfaces, but its accuracy is questionable for a very rough surface in which the correlation length and rms height are the same order of dimension as the tip of stylus.

An electron microscope has a high resolution and is useful for measuring the one-dimensional cross-section, but it is a destructive testing method. A newly developed tunneling electron microscope (STM) which has a high resolution and is capable for scanning a sample in two-dimensions, may be suited for obtaining the profile of a very rough surface.

Optical experiments involving discrete random media are frequently conducted with latex microspheres suspended in water [6,7]. The fractional volume density or particle concentration is controlled by diluting the original solution with distilled water and a slight amount of detergent. A wide range of mean diameters with a narrow standard deviation is available from manufactures which also supply the particle-size distribution and index of refraction at different wavelengths. During the experiments, latex particles must be randomly distributed and suspended in water without a substantial amount of settling. This requirement excludes particles for which the density is substantially different from that of water. Although the latex spheres from Dow Chemical have a density of 1.03 to 1.05 g/cm³, the range of index refraction at optical wavelength is also limited to 1.5 to 1.6. Because water has an index of refraction of 1.33 at optical wavelengths, the latex particles suspended in water have a relative index of refraction of only 1.22. If varying the fractional volume is not required and a high concentration is desired, a very high concentration of different index of refraction can be created by packing microspheres [2].

3. Experimental Systems

3.1 Introduction

In general, experimental systems for laboratory use are operated in less severe environmental conditions than outdoor systems. The temperature and mechanical stability required for the outdoor systems is usually not critical for laboratory experiments. The experimental systems, therefore, can be designed to be flexible and to incorporate state-of-the art instruments or components without testing their reliability under severe conditions. The wideband MMW bistatic radar system described in the following section is flexible and powerful enough for studying the MMW scattering from rough surfaces, but it is not

practical for outdoors. MMW radars designed for outdoor experiments are described in detail elsewhere [30, 31, 37]. Because the experimental results presented in Section 4 are limited to the microwave and MMW regions, the systems for the light scattering experiments are not included.

3.2 VNWA as an Microwave and MMW Receiver

The modern vector network analyzers (VNWA) such as an HP8510 are frequently used as a receiver of the scatterometer [30, 34]. A VNWA with its built-in functions provides most of the operations necessary for the receiver including signal detection, signal processing and computer interface. Compared to the dedicated microwave receivers, the VNWA based systems offer flexibility, ability to do sophisticated signal processing and a user friendly interface. Data acquisition and computer-control become particularly straight forward with its built-in GPIB interface and software. Figure 3.1 shows a simple radar system with an HP8510 VNWA [32]. The highest frequency is usually determined by the sweeper frequency, if the sweeper signal output is used as a transmitter. If a higher frequency range is needed than that of the sweeper output, a radar front-end must be added to the system with VNWA as an IF signal receiver.

In general, a measurement conducted in an enclosed room or in a limited space contains a significant amount of undesired noise due to the reflection from walls and other structures in addition to the direct antenna coupling. If the distance from the antenna to the target is less than a few meters, it is difficult to use a hardware gating circuit based on fast microwave PIN or GaAs switches. In this situation, the ability to do sophisticated signal processing on VNWA becomes essential for an accurate measurement of target response. A simple technique to reduce the noise is to subtract noise (room response without a target) from the received signal, known as the trace math operation on a Hewlett Packard VNWA. As long as the background room response is stationary, this is quite effective. However, if the room response is changed, e.g., by moving a target pedestal, the noise level may increase significantly.

A more robust method to reduce the background noise is the time gating function available on a VNWA. Because the VNWA measures both the magnitude and phase of the received signal as a function of

frequency, the Fourier transform of the received signal gives the time-domain responses of a target. If the target response is separated from the signal reflected from the walls and other structures in the time-domain data, the time gating function and inverse Fourier transform on the time gated signal can effectively reduce the noise in the frequency response. The VNWA responses with and without time gating functions are shown in Fig. 3.2. The software time gating is a very useful and powerful technique, but it is important to understand its limitation for the scatterometers. Because the software gating is a signal processing technique, the target must be stationary during the source sweep period. If the target motion is appreciable during the sweep time which is usually from 100 msec to 1 sec, the phase relationship at different frequencies will be destroyed and the Fourier transform may produce erroneous results. Because the phase change from motion is much more sensitive at a high frequency than at a low frequency, the mechanical stability becomes crucial for the MMW radars.

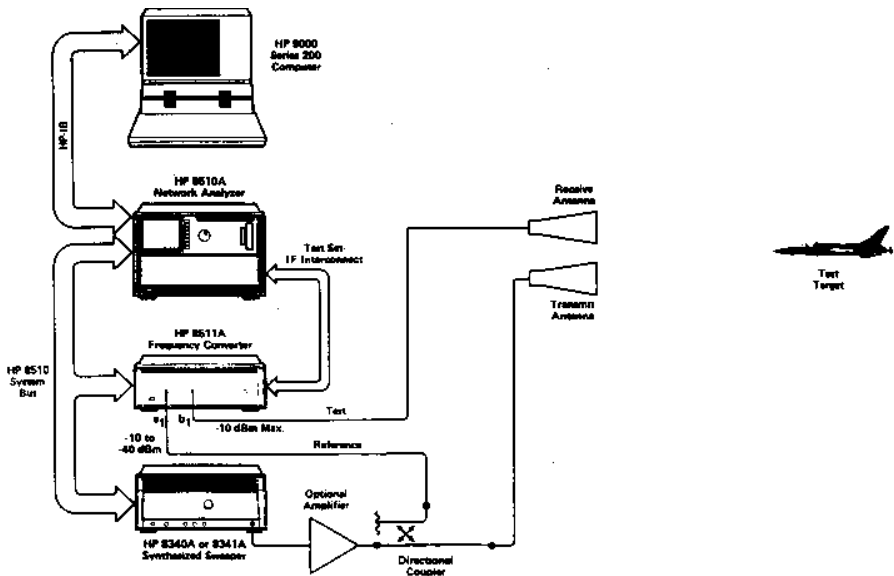


Figure 3-1. RCS measurement configuration with VNWA. (from Hewlett Packard Product Note 8510-2)

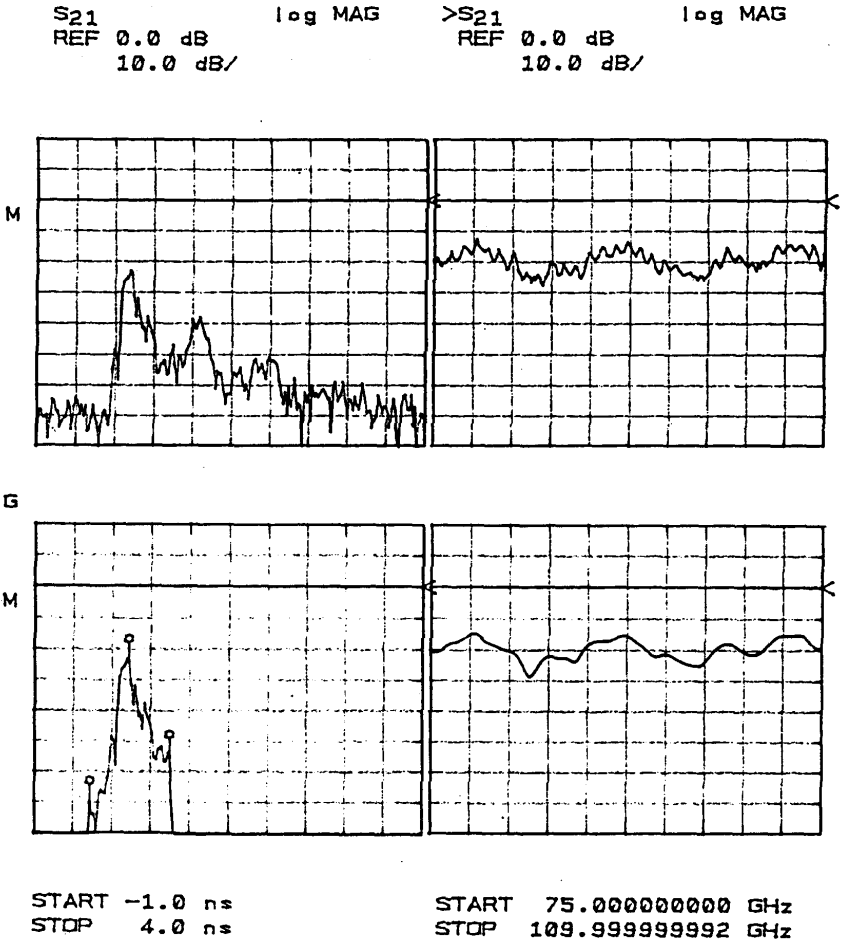


Figure 3-2. Time domain responses of a target without and with the time gating function. (from Hewlett Packard Product Note 8510-2)

3.3 MMW Systems

The frequency range of a VNWA is usually limited to the microwave region. To design a MMW scatterometer with a VNWA, the frequency conversion method such as up/down-conversion and signal multiplication should be added to the radar front-end and a VNWA should be used as the IF signal receiver. The up/down-conversion method shown in Fig. 3.3 is suited for a system that requires separation of the radar front-end from the VNWA. The RF transmitted signal is created by mixing (up-conversion) the MMW LO signal with the IF from the VNWA. The received RF is mixed with the same MMW LO and down-converted to the IF signal. Since the same MMW LO is used for both up- and down-conversions, the phase coherence is maintained between the transmitted and received RF signals. If a fundamental mixer is used for up/down-conversion, a conversion loss of less than 8 dB can be achieved. Because MMW RF and LO signals are contained in the radar front-end and the IF signal has a narrow bandwidth centered at several GHz, the radar front-end can be placed some distance from the IF receiver. Therefore, MMW radars based on the up/down-conversion are suited for outdoor track mounted scatterometers in which the MMW front-end is located at the end of a long boom [30]. Although designing a system with a wide bandwidth is feasible with the up/down-conversion method, the IF bandwidth is usually limited to 1 to 2 GHz. If an ultra wide bandwidth is required at the MMW region, the source signal multiplication method described in the following section is best suited.

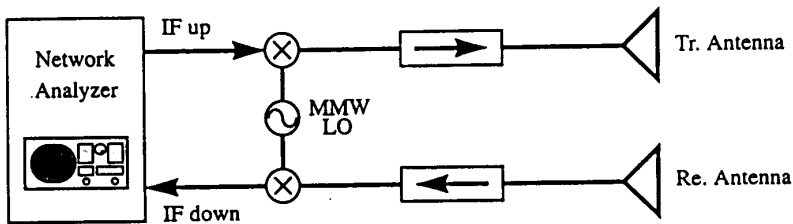
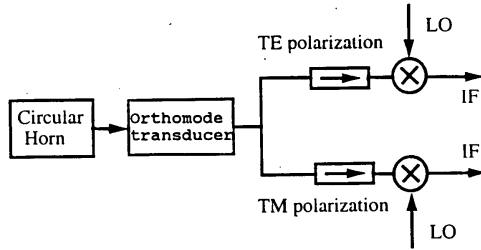


Figure 3-3. Simplified block diagram of a radar front-end with up/down converters.



(a) Receiver configuration

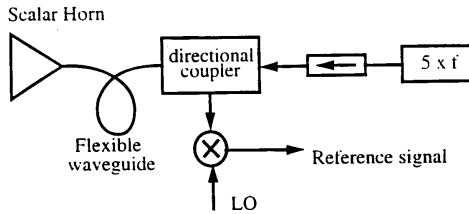


Figure 3-4. Simplified block diagram of the receiver and the transmitter.

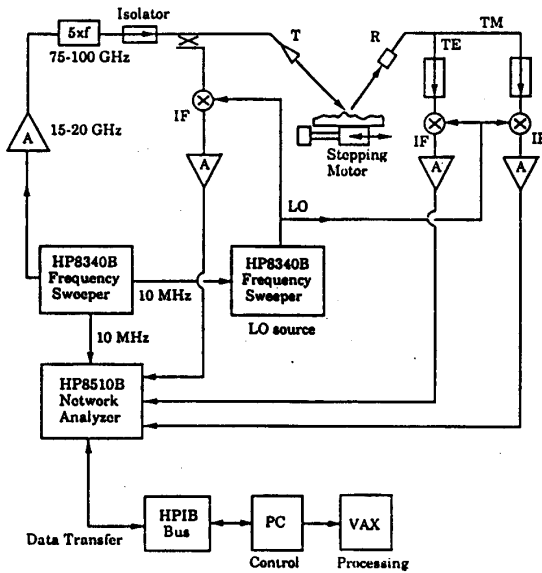


Figure 3-5. Simplified block diagram of the millimeter-wave experimental setup.

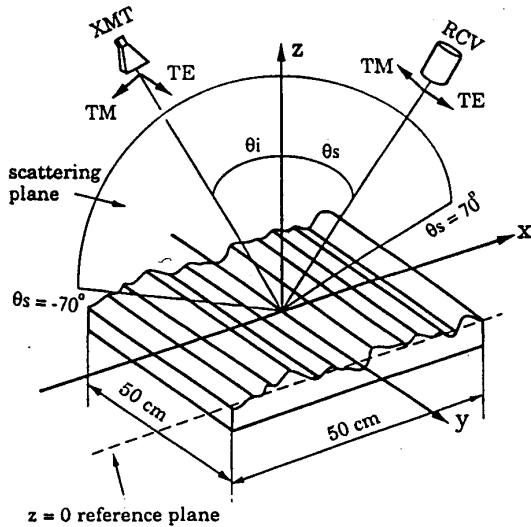


Figure 3-6. Simplified geometry of the scattering experiment for 1-D rough surface scattering.

A millimeter-wave vector network analyzer using the HP8510 and source signal multiplication method was introduced in 1986 [33]. The HP8510B MMW system is designed for flexibility and expandability, and it is available up to the W-band (75-110 GHz). The frequency band can be easily changed by replacing a source multiplier and harmonic mixers. The available source power, however, is limited due to the high conversion loss in the multiplier. For example, the original W-band source with a x5 multiplier had an output power of only -10 dBm. In addition, the S/N ratio is severely affected by the high conversion loss in harmonic mixers. The harmonic mixer at W-band, which uses either 16th or 18th harmonics, has a conversion loss of 30-40 dB. Because of the limited S/N ratio and internal reflections, the HP8510 MMW system is difficult to use without proper calibration. To improve the S/N ratio, the HP8510 MMW system must be operated in the step mode rather than the sweep mode at W-band which results in a significant increase in measurement time. Consequently, the radar system based on the HP8510 MMW system does not work very well if a target is not stationary for a long period of time. If, however, ultra wide bandwidth and flexibility are required at the W-band, the scatterometer based on the HP8510 MMW system is a good choice.

The MMW bistatic scatterometer at the University of Washington is based on the HP8510B MMW VNWA [34]. Extensive modifications were made to the front-end part of the system to convert it to a fully polarimetric scatterometer setup. In Figures 3.4–3.6, a simplified layout of the millimeter-wave scatterometer is shown. The HP83621 synthesized frequency sweeper generates a microwave signal from 12.5 to 18.3 GHz. The amplified and frequency-leveled microwave signal is then multiplied by 6 to the MMW frequency, 75–110 GHz. Unlike the original source module, the new HP83558 source module is capable of producing more than 0 dBm output at the W-band. In a fully polarimetric operation, the transmitted signal polarization is controlled by the rotational angle of a $\lambda/2$ wave plate in front of the transmitting antenna. The reference signal, a_1 , and the two outputs, b_1 and b_2 , are generated using a superheterodyne detection method with harmonic mixers. The two orthogonal polarizations received by the dual polarized receiving antenna are down converted by harmonic mixers with a LO microwave signal from an HP8341B synthesized frequency sweeper. This second sweeper is coherently phase-locked at all frequencies with the source sweeper. The resulting IF signal is amplified by a low-noise IF amplifier and input to the network analyzer. All real-time signal processing on the measurements is carried out by an HP8510B millimeter-wave VNWA. The frequency and output power of frequency synthesized sweepers are controlled by the HP8510B without the need of an external computer.

3.4 Calibration of the MMW Systems

Experimental systems must be calibrated to conduct quantitative analysis of the measured data. In the microwave and MMW regions, the magnitude calibration known as the RCS (radar cross section) calibration, is done by measuring a target of known RCS, such as spheres and trihedrals. Using the radar equation and the RCS of a known target, the RCS calibration determines the constant K which includes unknown parameters, such as the antenna gains and transmitted power [35]. The unknown target RCS is then given by the received power, constant K and the distance to the target. The MMW system described in Section 3.2 uses a large flat conducting plate and the “*Thru*” calibration on the HP8510 to correct the system responses of the V and H channels. A qualitative relationship between the measured cross section

including the effects of the beam width and the true 2-D normalized rough surface cross section will be considered here. Since the scattering cross sections of the rough surfaces are normalized with the specular power scattered from a perfectly conducting flat surface, the ratio of the power received from a rough surface to that from a flat surface is needed. If the flat surface is much larger than the illumination area of both antennas, the image method can be used to compute the power received. Using the radar equation [35], the total power received from a flat perfect conductor can be written as,

$$P_o = P_t \frac{\lambda^2}{(4\pi)^2} \frac{G_1 G_2}{(R_1 + R_2)^2} \quad (16)$$

where R_1 and G_1 are the antenna range and the antenna gain of the transmitter and R_2 and G_2 are those of the receiving antenna. The total power reflected from an extended body, such as a rough surface, is given by the radiation integral

$$P_r = P_t \frac{\lambda^2}{(4\pi)^3} \int \frac{G_1 G_2 \sigma}{R_1^2 R_2^2} ds \quad (17)$$

In general, the parameters within the surface integral depend on the local coordinates of the surface. To simplify the computation in order to gain additional physical insights, some approximations are used. For a Lambertian surface, σ is constant. Furthermore, if both antennas are far from the rough surface, then R_1, R_2 do not change appreciably at the edge of the illumination area. The received power under these assumptions becomes

$$P_r = P_t \frac{\lambda^2}{(4\pi)^3} \frac{\sigma}{R_1^2 R_2^2} \int G_1 G_2 ds \quad (18)$$

For a beam limited radiator, it is possible to approximate the above surface integral in the following way. The gain functions of both antennas are slowly varying functions of angle within the HPBW (half-power beamwidth) illumination cone. Therefore, the antenna gain can be assumed to be constant within the HPBW footprint and zero everywhere else. Given the common illuminated surface area of both antennas, the surface integral can be approximated as

$$\int G_1 G_2 ds \simeq G_1 G_2 \frac{\pi R_2^2 \theta_r^2}{4} \frac{1}{\cos \theta_s} \quad (19)$$

Therefore, the received power can be written as

$$P_r \simeq P_t \frac{\lambda^2}{(4\pi)^3} \frac{G_1 G_2 \sigma}{R_1^2 R_2^2} \left(\frac{\pi R_2^2 \theta_r^2}{4} \frac{1}{\cos \theta_s} \right) \quad (20)$$

If $R_1 = R_2$, the ratio of the received power from an arbitrary surface to the received power from a conducting flat surface is

$$\frac{P_r}{P_o} = \sigma \frac{\theta_r^2}{4 \cos \theta_s} \quad (21)$$

The above power ratio describes the scattering cross section as measured by the millimeter wave system. Only the effect of the beam width of the receiver is included since, for all practical purposes, the incident radiation is constant across the illuminated area of the receiver.

In addition to the RCS calibration, fully polarimetric radars require phase calibration to obtain the relative phase relationship of two orthogonal polarizations [36–37]. At the MMW frequency the depolarization due to random media is quite appreciable. Furthermore, it has been shown that the useful phase information in the scattered field is contained in the phase difference between the two co-polarized components, VV (V-pol. transmit and V-pol. receive) and HH (H-pol. transmit and H-pol. receive) [29, 37]. Because the isolation between V and H channels of a high quality dual-polarized antenna is easily more than 20 dB, a simple magnitude and phase calibration of two co-polarized channels is usually sufficient to obtain the magnitude of co- and cross-polarized components (VV, HH, VH, and HV) as well as the phase difference of two co-polarizations. For the MMW system described in Section 3.3, this is done by performing the “*Thru*” calibration to both VV and HH channels. The polarization response, in particular, the cross-polarization response can be improved significantly by the error correction technique which compensates for the antenna distortion matrix [37–38].

4. Experimental Results on Rough Surfaces and Discrete Random Media

4.1 Introduction

During the past several years, we have conducted a wide variety of MMW experiments using the system and the random media fabrication techniques described in Sections 2 and 3. We have demonstrated that the MMW system is very useful for careful comparisons between the experimental data and the numerical and theoretical calculations. In this section, therefore, we will present some of these results. In Section 4.2, the advantages of fabricating rough surfaces using a CAD/CAM system will be shown. The scattering characteristics of rough surfaces with different correlation functions are measured with the MMW system, and the results are compared with the numerical calculations. Although some progress has been made recently, the numerical simulation of vector wave scattering from 2-D rough surfaces is still a difficult task [39]. To verify the theoretical calculation, therefore, it is essential to conduct carefully controlled experiments in which all the parameters are known. MMW scattering from 2-D rough surfaces will be discussed in Section 4-3. The comparison between experimental data and theory will be given in this book [40]. In Section 4.4, the ability to calculate the time-domain response from the wide-band frequency-domain data will be demonstrated. The velocities of coherent and incoherent fields are measured as a function of frequency and a sharp decrease of the incoherent velocity in the Mie resonance region will be shown.

4.2 Effects of the Surface Correlation Functions on the MMW Scattering Characteristics

Natural surfaces often contain more high frequency components than those obtained from the Gaussian correlation function. The roughness of natural surfaces is more accurately described with an exponential correlation function or power law spectral density [41]. Since both experimental and numerical studies show that backscattering enhancement increases as the roughness of the surface increases,

the rough profiles or high frequency components in a spectral density are believed to be an important factor in backscattering enhancement. Because of this, there has been strong interest in studying scattering from surfaces whose spectral density has higher frequency components than that of the Gaussian spectral density. Some preliminary numerical studies were conducted for surfaces with non-Gaussian roughness spectral density, but no experimental studies have been reported [42]. This lack of experimental study is primarily due to the difficulty of fabricating surfaces with a non-Gaussian spectral density at the optical wavelength. If the experiment is conducted in the MMW region, however, a surface of desired statistics can be created with very good accuracy using the CAD/CAM system described in Section 3.

In this section we will present the bistatic scattering characteristics of surfaces with Gaussian autocorrelation function and power law spectral density. MMW scattering from one-dimensional surfaces with a power law spectral density $n=2$ is compared with those with a Gaussian spectral density. A photograph of two surfaces with Gaussian and power law spectral densities is shown in Fig. 4-1. The same seed number is used for the random number generator to compare two profiles. Conducting surfaces with an rms height $h=3$ mm and correlation lengths $l=3, 6,$ and 9 mm were created using the method described in Section 2. The corresponding rms slopes were $m=1.41, 0.707,$ and $0.47,$ respectively. Experimental results were compared with the numerical simulations based on the Monte-Carlo solution for the integral equation [42, 20, 34]. Figure 4-2 shows the normalized cross section as a function of scattering angle and frequency for the power law spectrum surfaces with $h=3$ mm and $l=9$ mm ($m=0.47$), $h=3$ mm and $l=6$ mm ($m=0.707$), and $h=3$ mm and $l=3$ mm ($m=1.41$), respectively. As expected, when the surface correlation length decreases, the scattered intensity in the backscattering direction ($\theta_s = -20^\circ$) increased significantly.

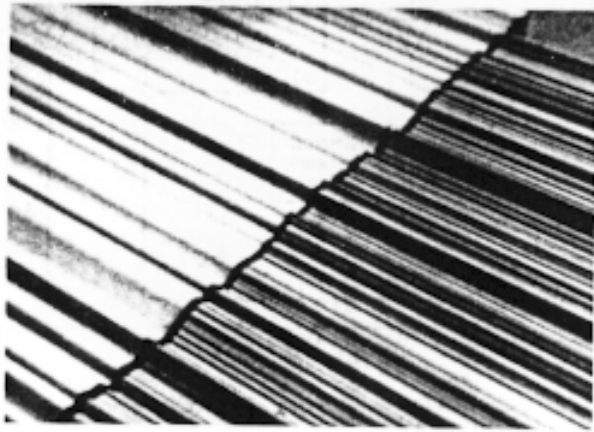


Figure 4-1. Photograph of two surfaces with Gaussian (left) and power law (right) spectral densities.

Figure 4-3 shows both the measured and numerical simulation data at 100 GHz ($\lambda = 3\text{mm}$) for a Gaussian correlation function with $h/\lambda = 1$ and $l/\lambda = 3$ ($m = 0.47$), $h/\lambda = 1$ and $l/\lambda = 2$ ($m = 0.707$), and $h/\lambda = 1$ and $l/\lambda = 1$ ($m = 1.41$), respectively. Figure 4-4 shows the same data for surfaces with a power law spectral density. From the previous numerical studies, backscattering enhancement is known to occur when the rms slope approaches 1 for surfaces with a Gaussian correlation function and $h/\lambda = 1$ [52]. This is clearly shown in Figure 4-3 in which backscattering enhancement is not visible for $h/\lambda = 1$ and $l/\lambda = 2$ (Fig. 4-3-b: $m = 0.707$); whereas the data for $h/\lambda = 1$ and $l/\lambda = 1$ (Fig. 4-3-c: $m = 1.41$) has backscattering enhancement. However, both experimental and numerical results reveal that surfaces with a power law spectral density have backscattering enhancement for $h/\lambda = 1$ and $l/\lambda = 2$ ($m = 0.707$) as shown in Figure 4-4-b. Since natural surfaces are known to have a correlation function close to an exponential correlation function, it is expected that backscattering enhancement will occur even for a small rms slope.

Figure 4-2. Measured data for $\theta_i = 20^\circ$. Observation angle $\theta_s = -20^\circ$ corresponds to the backscattering direction. (a) power law: $h = 3$ mm and $l = 9$ mm ($m = 0.47$), (b) power law: $h = 3$ mm and $l = 6$ mm ($m = 0.707$), and (c) power law: $h = 3$ mm and $l = 3$ mm ($m = 1.41$).

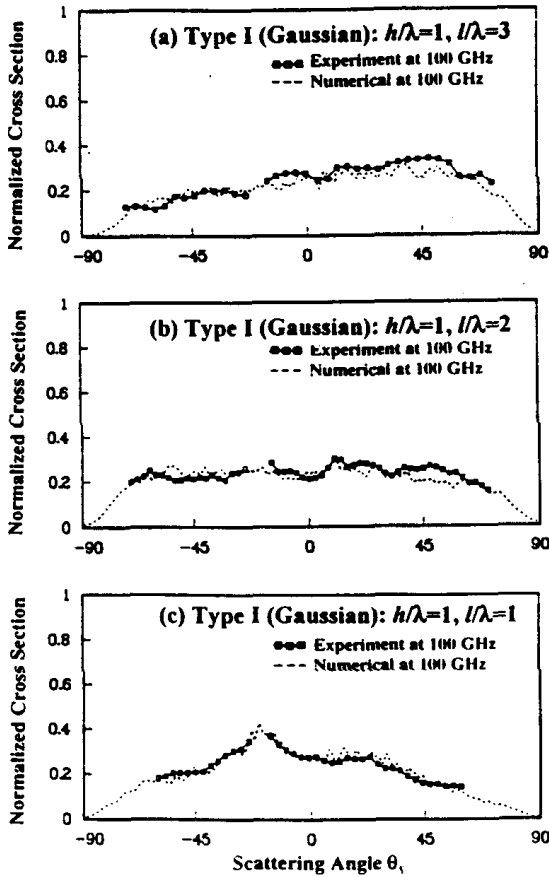


Figure 4-3. Measured and numerical results at 100 GHz for $\theta_i = 20^\circ$. $\theta_s = -20^\circ$ corresponds to the backscattering direction. (a) Gaussian: $h = \lambda = 1$ and $l/\lambda = 3$ ($m = 0.47$), (b) Gaussian: $h/\lambda = 1$ and $l/\lambda = 2$ ($m = 0.707$), and (c) Gaussian: $h/\lambda = 1$ and $l/\lambda = 1$ ($m = 1.41$). Cylindrical phase front is used for the numerical simulations.

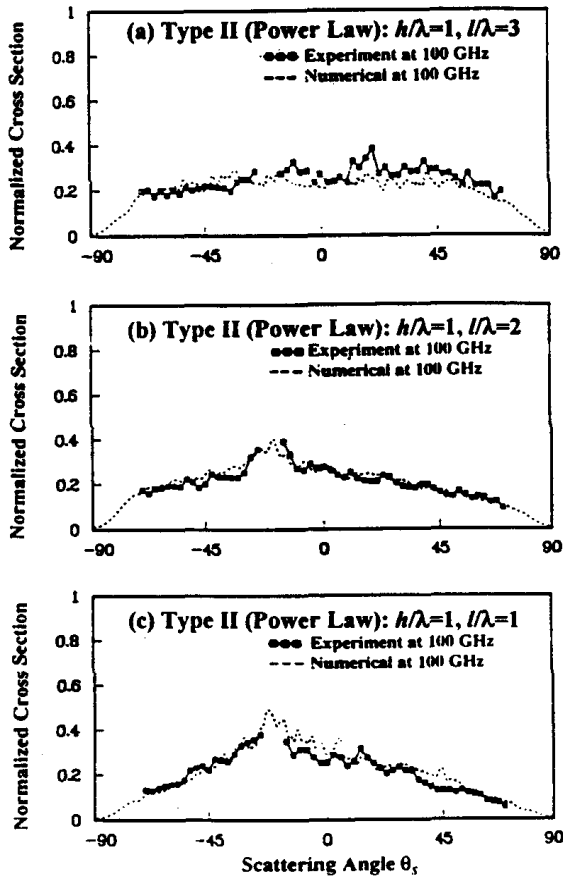


Figure 4-4. Measured and numerical results at 100 GHz for $\theta_i = 20^\circ$. $\theta_s = -20^\circ$ corresponds to the backscattering direction. (a) power law: $h/\lambda = 1$ and $h/\lambda = 3$ ($m = 0.47$), (b) power law: $h/\lambda = 1$ and $h/\lambda = 2$ ($m = 0.707$), and (c) power law: $h/\lambda = 1$ and $h/\lambda = 1$ ($m = 1.41$). Cylindrical phase front is used for the numerical simulations.

4.3 MMW Scattering from 2-Dimensional Rough Surfaces

In order to investigate the scattering characteristics of 2-D rough surfaces, several different types of rough surfaces are fabricated for measurement. All the surfaces have Gaussian power spectrum density with normal height distribution. The type I surface has an rms height $h=3$ mm and correlation length $l_x = l_y = 12$ mm, where the rms slope $m_x = m_y = 0.353$. The type II surface has an $h=3$ mm and $l_x = l_y = 9$ mm ($m_x = m_y = 0.47$). Previous research on experimental and numerical studies of 1-dimensional surfaces with the same characteristics as Type I and II surfaces showed no visible enhancement [34,53]. The type III surface has an $h=3$ mm and $l_x = l_y = 6$ mm ($m_x = m_y = 0.707$). Surface type IV has an $h=3$ mm and $l_x = l_y = 4.24$ mm ($m_x = m_y = 1$). It will be shown later that, at this particular rms slope, the enhancement is quite evident for both copolarized and cross-polarized returns. All surface types are isotropic. To investigate the effect of surface anisotropy on the scattering characteristics, surfaces with anisotropic correlations functions are also fabricated and measured [34].

Both the copolarized and cross-polarized cross sections are measured for the incident angle $\theta_i = -20^\circ$. The range of observation angles is from -70° to $+70^\circ$, with -20° being the backscattered direction and $+20^\circ$ being the specular direction. Measurements are obtained for TE incident polarization. Figures 4-5 to 4-8 show both the copolarized and cross-polarized cross sections as a function of frequency and observation angles for surface types I, II, III, and IV. The cross section is calculated from the measured power using Eq. (21). To smooth out the data, a moving average on both angle (window size= 4°) and frequency (window size=2.5 GHz) is performed.

Figure 4-5. Co- and cross-polarized cross section for Type I surface. Scattering angle $\theta_s = -20^\circ$ corresponds to the backscattering direction. $h = 3$ mm and $l = 12$ mm ($m = 0.353$).

Figure 4-6. Co- and cross-polarized cross section for Type II surface. Scattering angle $\theta_s = -20^\circ$ corresponds to the backscattering direction. $h = 3$ mm and $l = 9$ mm ($m = 0.47$).

Figure 4-7. Co- and cross-polarized cross section for Type III surface. Scattering angle $\theta_s = -20^\circ$ corresponds to the backscattering direction. $h = 3$ mm and $l = 6$ mm ($m = 0.707$).

Figure 4-8. Co- and cross-polarized cross section for Type IV surface. Scattering angle $\theta_s = -20^\circ$ corresponds to the backscattering direction. $h = 3$ mm and $l = 4.24$ mm ($m = 1$).

As expected, surface type I shows strong forward scattering and no visible backscattering enhancement effect. On the other hand, surface types III and IV show very strong backscattering enhancement for both copolarized and cross-polarized returns. The angular width of the backscattered peak is narrower in the cross-polarized case which can be explained qualitatively by the contributions of different scattering orders. In the case of copolarized returns, the cross section mainly consists of single and double scatterings. Since the intensity of first-order scattering is mostly diffusive due to weak localization, the copolarized enhancement has a broad angular width, in the range of 10° to 20° . In contrast, the cross-polarized peak is mostly due to the coherent addition of the double scattered rays. The absence of first-order scattered energy and the phase matching condition for the second-order ladder and cyclical terms reduce the overall angular width of the backscattered peak [43]. The comparison between the experimental results and the second-order Kirchhoff calculation is presented by Ishimaru et al. in this book [40].

4.4 Velocity of Coherent and Incoherent Electromagnetic Waves in Dense Strongly Scattering Media

Recently, it was shown experimentally and theoretically that the speed of light in strongly scattering media can be reduced to a fraction of the vacuum speed of light [8]. Experimentally, the transport mean free path ℓ is obtained from steady-state measurements and the diffusion coefficient D is obtained from dynamic measurements. According to $D = v\ell/3$, the velocity v is found to be very low, particularly in the region of resonance scattering of particles where the stored energy is large. It was explained that the velocity v is neither phase nor group velocity, but the energy velocity v_E , and this was confirmed by theoretical study of v_E [8].

We will show additional confirmation of this low speed by performing a pulse propagation experiment at microwave frequencies [45]. Using a network analyzer, frequency and time-domain experiments are conducted for a broad-band microwave signal propagating through randomly distributed glass spheres whose sizes are close to a wavelength such that resonance scattering takes place. The transmitted pulse is then decomposed into coherent and incoherent pulses. It is found that the speed, at which 50% of the transmitted incoherent power arrives,

is consistent with energy velocity v_E given previously [8]. Since the incoherent wave in a dense medium is the diffuse wave, the velocity presented here corresponds to the velocity of the diffuse wave and it is different from the ballistic velocity. However, it is found that the speed of the coherent pulse is nearly constant and is different from the phase, group, or energy velocity.

The random medium consists of 5.73 mm glass spheres embedded in layers of styrofoam sheets with the fractional volume of 11% [25]. The locations of the glass spheres on styrofoam sheets are generated by a random number generator. The extinction cross-section of 5.73 mm glass spheres as a function of frequency is shown in Fig. 4-9. The 10-20 GHz band corresponds to the transition from the Rayleigh to the Mie scattering region and the 25-40 GHz band corresponds to the Mie resonance scattering regions. To obtain the statistical data, the different medium configurations are created by shuffling the styrofoam layers. The results presented here are based on 100 samples.

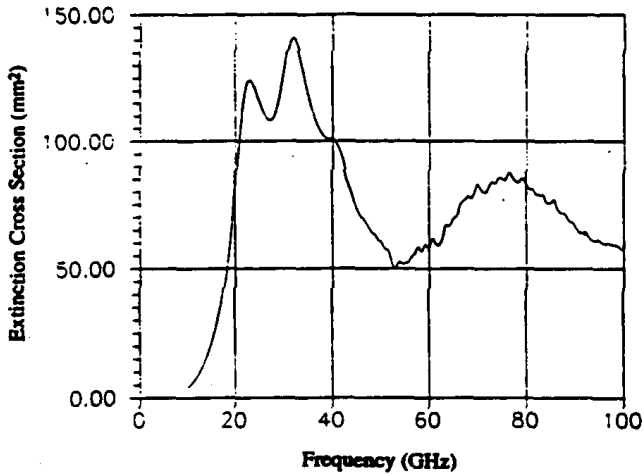


Figure 4-9. Extinction cross section of glass spheres. The index of refraction is $n = 2.15 + i0.01$ and the average diameter is 5.73mm.

The electromagnetic waves propagating through a random medium can be separated into coherent (average) and incoherent (fluctuating) waves as shown below [1].

$$E_{\text{total}}(f) = E_{\text{coherent}}(f) + E_{\text{incoherent}}(f) \quad (22)$$

The ensemble average of the incoherent waves is zero, but the incoherent intensity which is defined as $\langle |E_{\text{incoherent}}(f)|^2 \rangle$, is non-zero. The time-domain response of the coherent waves is calculated by taking the inverse Fourier transform of an average field $E_{\text{coherent}}(f)$. To obtain the time-domain response of the incoherent waves, the following steps are involved. First, the incoherent field is obtained by subtracting the average (coherent) field from the total field. Second, the inverse Fourier transform is performed on this data to get the time-domain response of each incoherent wave. Finally, an average over many realizations is obtained to get the time-domain response of the incoherent waves. These operations can be described as

$$\text{Time Response of Coherent Waves} = |\mathcal{F}^{-1}[E_{\text{coherent}}(f)]| \quad (23)$$

$$\text{Time Response of Incoherent Waves} = \langle |\mathcal{F}^{-1}[E_{\text{incoherent}}(f)]| \rangle \quad (24)$$

Figures 4–10 and 4–11 show the time-domain responses of the coherent and incoherent waves at eight different frequency bands between 10 and 40 GHz. The magnitude is normalized to its peak value to compare the pulse arrival time and broadening. Each time domain response is obtained using a 2.5 GHz bandwidth centered at f_c . All eight responses of the coherent waves are very similar showing that these coherent waves are propagating with the same velocity. If the pulse arrival time is defined as a time at which 50% of the energy arrives, the velocity of the coherent waves is almost constant. The pulse arrival time of the incoherent waves, shown in Fig. 4–11, displays a strong frequency dependence, and the delay increases as the center frequency changes from 11.25 to 18.65 GHz. The time responses between 31–25 and 38.65 GHz also show a substantial amount of pulse broadening.

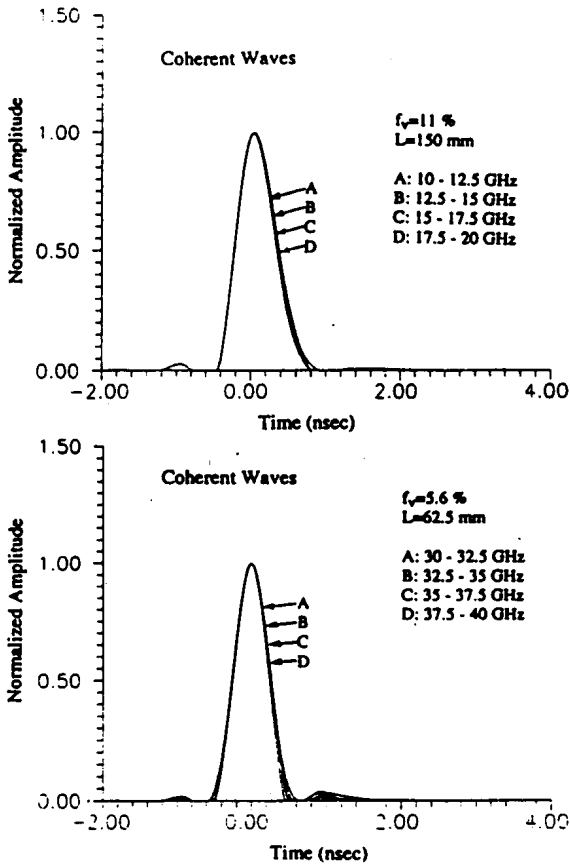


Figure 4-10. Time-domain responses of coherent waves. Frequency ranges are from 10 to 20 GHz (top) and 30 to 40 GHz (bottom).

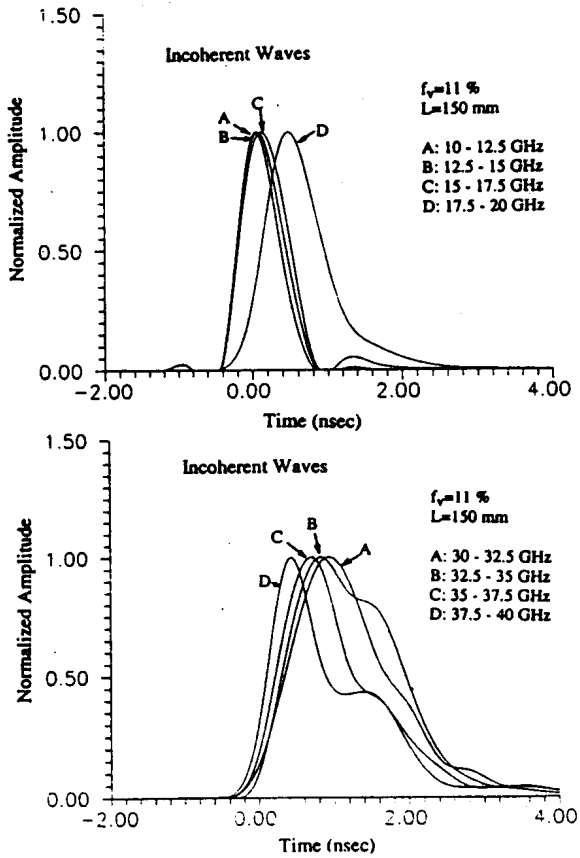


Figure 4-11. Time-domain responses of incoherent waves. Frequency ranges are from 10 to 20 GHz (top) and 30 to 40 GHz (bottom).

In Figure 4-12, the time delay of the incoherent waves is shown as a function of center frequency f_o . The pulse arrival time is obtained using the 50% energy point because this method is less sensitive to the noise than the arrival time of peak magnitude. If the pulse arrival time is defined as a position of peak magnitude, the time delay becomes less than that of the data shown in Fig. 4-12. No delay (0 nsec) corresponds to the pulse arrival time through styrofoam layers without glass spheres.

Figure 4-12. Time delay of the incoherent waves as a function of center frequency f_o .

Figure 4-13. Normalized velocity of the incoherent waves as a function of center frequency f_o . Solid line is the energy velocity given by Eq. (4.4). A spike at 21 GHz is a numerical error due to the difficulty of evaluation the numerical differentiation.

Figure 4-13 shows the velocity of the incoherent waves normalized to the free space velocity. The fractional volume is 11%. It is clear that in this dense scattering medium, the velocity decreases rapidly in the Rayleigh to Mie transition region and remains at about 30% to 40% of the free space value in the Mie resonance scattering region. The experimental results are compared with the energy velocity of waves propagating through randomly distributed spherical particles shown below [8].

$$V_E = \frac{C_o}{\left(\frac{1 + \frac{3f_v}{4x^2} \sum_{n=1}^{\infty} (2n+1) \left(\frac{\frac{d}{dx} \text{Im}(a_n)}{1 - 2\text{Re}(a_n)} + \frac{\frac{d}{dx} \text{Im}(b_n)}{1 - 2\text{Re}(b_n)} \right) - \frac{1}{2} f_v A}{\sqrt{1 + f_v A}} \right)} \quad (25)$$

$$A = \frac{3}{2x^3} \sum_{n=1}^{\infty} (2n+1) [\text{Im}(a_n + b_n)]$$

where a_n and b_n are Mie coefficients, f_v is a fractional volume, x is a size parameter, and C_o is a free space light velocity. The above expression is evaluated for the fractional volume of 11% and the results are shown in Fig. 4-13. Because the measured velocity depends on how we define the pulse arrival time and Eq. (25) does not define the pulse arrival time, the discrepancy in Fig. 4-13 may be due to the definition of pulse arrival time. Also Eq. (25) is evaluated using mono-dispersive particles (a single particle size) and at a given frequency; whereas, the experimental data is obtained with a 2.5 GHz bandwidth and poly-dispersive particles. Nevertheless, the trend of the experimental results is similar to the energy velocity given by Eq. (25).

The velocity of electromagnetic waves in random media has been studied extensively in the past. Optical experiments using a picosecond laser and polystyrene microspheres suspended in water were conducted by several research groups [47-48]. Although these experiments were conducted with several different particle sizes, little experimental data

are available for the wide continuous range of size parameters. In particular, the diffuse wave velocity in the Mie resonance scattering region has not been studied extensively. In addition, it is difficult to separate coherent waves from incoherent waves in optical experiments. In this section, we show the advantages of conducting microwave pulse propagation experiments using a wide-band microwave system (10-20 and 25-40 GHz band) and glass spheres embedded in styrofoam sheets. This is a dense scattering medium with the fractional volume of 11%. The frequency and particle size were chosen so that the experiment covers the Rayleigh-Mie transition region and Mie resonance scattering region.

5. Conclusion

Understanding electromagnetic wave interaction with random media is important not only in remote sensing of geophysical media but in many other areas of science and engineering. New phenomena, such as backscattering enhancement, weak and strong localization, and resonance localization cannot be explained by classical theories which ignore the correlation of particles and interaction of waves propagating in the opposite directions. A new class of microwave and optical materials which utilize the *strong Anderson localization* have been developed [49–50]. We have shown that a MMW scatterometer combined with a random media fabrication method is a powerful tool for studying wave scattering from discrete random media and rough surfaces. In addition to the results presented here, the system has been used for studying the angular correlation of wave scattering from rough surfaces, phase statistics of the two co-polarized waves scattered from 2-D rough surfaces, pulse broadening, angular and polarization memory effects, coherent and incoherent waves in random media, and phase and attenuation constants of the coherent wave [28,34,51].

References

1. Ishimaru, A., *Electromagnetic Wave Propagation, Radiation and Scattering*, Vol. 2, New York: Academic Press, 1978.
2. John, S., "Localization of light," *Physics Today*, Vol. 44, No. 5, 32–40, 1991.
3. Sheng, P.(ed), *Scattering and Localization of Classical Waves in Random Media*, Singapore, World Scientific Publishing Co, 1990.
4. Tsang, L., J. A. Kong, and R. T. Shin, *Theory of Microwave Remote Sensing*, John Wiley and Sons, New York, 1985.
5. de Wolf, D. A., "Electromagnetic reflection from an extended turbulent medium: cumulative forward-scatter single-back-scatterer approximation," *IEEE Trans. Antennas Propag.*, AP-19, 254–262, 1971.
6. Kuga Y., and A. Ishimaru, "Retroreflectance from a dense distribution of spherical particles," *J. Opt. Soc. Am.*, A1, 831–835, 1984.
7. Wolf, P. E., and G. Maret, "Weak localization and coherent back-scattering of photons in disordered media," *Phys. Rev. Lett.*, Vol. 55, No. 24, 2696–2699, 1985.
8. van Aldaba, M. P., B. A. van Tiggelen, A. Lagandijk, and A. Tip, "Speed of propagation of classical waves in strongly scattering media," *Phys. Rev. Lett.*, Vol. 66, 3132, 1991.
9. Tsang, L., and A. Ishimaru, "Backscattering enhancement of random discrete scatterers," *J. Opt. Soc. Am.*, A1, 836–839, 1984.
10. Gehrels, T., T. Coffeen, and D. Owings, "Wavelength dependence of polarization. III. The lunar surface," *Astron. J.*, 69, 826–852, 1964.
11. Beard, C. L., T. H. Kays, and V. Twersky, "Scattering by random distribution of spheres vs. concentration," *IEEE Trans. on Antennas and Propagation*, AP-15, 99–118, 1967.
12. Beard, C. L., "Behavior of non-Rayleigh statistics of microwave forward scatter from a random water surface," *IEEE Trans. Antennas. Propagat.*, AP-15, 649–657, 1967.
13. Mendez, E. R., and K. A. O'Donnell, "Observation of depolarization and backscattering enhancement in light scattering from Gaussian random surfaces," *Optics Communications*, Vol. 61, No. 2, 91–95, 1987.

14. O'Donnell, K. A., and E. R. Mendez, "Experimental study of scattering from characterized random surfaces, *J. Opt. Soc. Am.*, A4, 1194-1205, 1987.
15. Gu, Z. H., R. S. Dummer, A. A. Maradudin, and A. McGurn, "Experimental study of the opposite effect in the scattering of light from a randomly rough metal surface," *Appl. Optics*, Vol. 28, 537-543, 1989.
16. Kim, M. J., J. C. Dainty, A. T. Friberg, and A. J. Sant, "Experimental study of enhanced backscattering from one- and two-dimensional random rough surfaces," *J. Opt. Soc. Am.*, Vol. A7, 569-577, 1990.
17. Phu, P., A. Ishimaru, and Y. Kuga, "Controlled millimeter wave experiments and numerical simulations on the enhanced backscattering from one-dimensional very rough surfaces," *Radio Science*, Vol. 28, 533-548, 1993.
18. Michel, T. R., M. E. Knotts, and K. A. O'Donnell, "Stokes matrix of a one-dimensional perfectly conducting surface," *J. Opt. Soc. Am.*, Vol. A9, 585-596, 1992.
19. Nito-Vesperinas, M., "Enhanced backscattering," *Optics and Photonics*, Vol. 1, No. 12.12, 50-52, 1990.
20. Thorsos, E. I., "The validity of the Kirchhoff approximation for rough surface scattering using a Gaussian roughness spectrum," *J. Acoust. Soc. Am.*, Vol. 83, No. 1, 78-92, 1988.
21. Oppenheim, A. V., and R. W. Schaffer, *Digital Signal Processing*, Prentice Hall, Inc., New Jersey, 1975.
22. Coons, S. A., "Surfaces for computer aided design of space forms," Rep. MAC-TR-41, Project MAX, MIT, Cambridge, MA, June 1967 (Available as AS-663-564 from Natl. Tech. Info. Serv., Springfield, VA.)
23. Olesten, N. O., *Numerical Control*, Wiley-Interscience, New York, 1970.
24. Olsen, R. L., and M. M. Z. Kharadly, "Experimental investigation of the scattering of electromagnetic waves from a model random medium of discrete scatterers, *Radio Science*, Vol. 11, 39-48, 1976.
25. Mandt, C. E., Y. Kuga, L. Tsang, and A. Ishimaru, "Microwave propagation and scattering in a dense distribution of non-tenuous spheres: Experiment and theory," *Waves in Random Media*, Vol. 2, No. 3, 225-234, 1992.

26. Bredow, J. R. Porco, and A. Fung, "Fully polarimetric measurements of robotically fabricated dense media targets," *Proceedings of IGARSS '94*, Pasadena, CA, July 1994.
27. Porco, R. L. and J. W. Bredow, "Robotic Aided Dense Medium Target Fabrication," *IEEE Trans. on Geoscience and Remote Sensing*, Vol. 32, 217–219, 1994.
28. Clayton, C., and Y. Kuga, "Bistatic scattering characteristics of dense randomly distributed cylinders," *Radio Science*, Vol. 30, No. 4, 817–826, 1995.
29. Ulaby, F. T., D. Held, M. C. Dobson, K. C. McDonald, and T. B. A. Senior, "Relating polarization phase difference of SAR signals to scene properties," *IEEE Trans. Geosci. Remote Sens.*, Vol. 25, No. 1, 83–92, 1987.
30. Ulaby, F. T., M. W. Whitt, and K. Sarabandi, "AVNA- based Polarimetric Scatterometers," *IEEE Antennas and Propagation Magazine*, 1990.
31. Mead, J. B., "Polarimetric Measurements of Foliage and Terrain at 225 GHz," Ph.D. Thesis, Univ. of Mass., 1989.
32. Hewlett Packard, Product Note, 8510-2, 1985.
33. Hewlett Packard, Product Note, 8510-12, 1987.
34. Phu, P., "MMW experiments and numerical studies on the enhanced backscattering from characterized very rough surfaces," Ph.D. Thesis, University of Washington, 1993.
35. Ulaby, F. T., R. K. Moore, and A. K. Fung, *Microwave Remote Sensing: Active and Passive, vol. II, Radar Remote Sensing and Surface Scattering and Emission Theory*, Artech House, Inc., Norwood, MA, 1986.
36. Barnes, R. M., "Polarimetric calibration using in-scene reflectors," Rep. TT-65, MIT Lincoln Lab, MA, 1986.
37. Ulaby, F. T., and C. Elachi (eds), *Radar Polarimetry for Geoscience Applications*, Artech House Inc., MA, 1990.
38. Riegger, S., W. Wiesbeck, and A. J. Sieber, "On the origin of cross polarization in remote sensing," Proceedings of IGARSS 87, Ann Arbor, MI, May 1987.
39. Tsang, L., C. H. Chan, H. Sangani, A. Ishimaru and P. Phu, "A banded matrix iterative approach to Monte Carlo simulations of large scale random rough surface scattering: TE case," *J. of Electromagnetic waves and applications*, Vol. 7, No. 9, 1185–1200, 1993.

40. Ishimaru, A., C. Le, Y. Kuga, and L. Ailes-Sengers, "Polarimetric scattering theory for high slope rough surfaces," *Progress in Electromagnetics Research*, PIER 14, 1–36, 1996.
41. Ogilvy, J. A. *Theory of Scattering from Random Rough Surfaces*, Adam Hilger, Bristol, England, 1991.
42. Chen, J. S., and A. Ishimaru, "Numerical simulation of the second-order Kirchhoff approximation from very rough surfaces and a study of backscattering enhancement," *J. Acoust. Soc. Am.*, Vol. 88, 1846–1850, 1990.
43. Ishimaru, A., and J. S. Chen, "Scattering from very rough metallic and dielectric surfaces: A theory based on the modified Kirchhoff approximation," *Waves Random Media*, Vol. 1, 21–34, 1991.
44. Kuga Y., J. Colburn, and P. Phu, "MMW scattering from one-dimensional surfaces of different surface correlation functions," *Waves Random Media*, Vol. 3, 101–110, 1993.
45. Kuga, Y., A. Ishimaru, and D. Rice, "Velocity of coherent and incoherent electromagnetic waves in a dense strongly scattering medium," *Phys. Rev. B.*, Vol. 48, 13155–13158, 1993.
46. Ishimaru, A., "Experimental and theoretical studies on enhanced backscattering from scatterers and rough surfaces," in *Scattering in Volumes and Surfaces*, M. Nieto-Vesperinas and J. C. Dainty (eds.), 1–15, Amsterdam, Elsevier Science Publishers, 1990.
47. Kuga, Y., A. Ishimaru, and A. P. Bruckner, "Experiments on picosecond pulse propagation in a diffuse medium," *J. of the Optical Society of American*, Vol. 73, No. 12, 1812–1815, 1983.
48. Zaccanti, G., P. Brusaglioni, A. Ismaelli, L. Carraresi, M. Gurioli, and Q. Wai, "Transmission of a pulsed thin light beam through thick turbid media: experimental results," *Applied Optics*, Vol. 31, No. 12, 2141–2147, 1992.
49. Yablonovith, E., and T. J. Gmitter, "Photonic band structure: the face-centered-cubic case," *Phys. Rev. Lett.*, Vol. 63, No. 18, 1950–195, 1989.
50. Yablonovith, E., T. J. Gmitter, R. D. Meade, A. M. Rappe, K. D. Brommer, and J. D. Joannopoulos, "Photonic band structure: the face-centered-cubic case," *Phys. Rev. Lett.* Vol. 67, No. 24, 3380–3383, 1991.
51. Kuga, Y., D. Rice, and R. West, "Propagation characteristics and velocity of the coherent wave in dense strongly scattering media," accepted by *IEEE Trans. Antennas and Propagation*, 1995.

52. Ishimaru, A., "Backscattering enhancement: From radar cross sections to electron and light localizations to rough surface scattering," *IEEE Ant. and Prop. Magazine*, Vol. 33, No. 5, 7–11, 1991.
53. Phu, P., A. Ishimaru, and Y. Kuga, "Copolarized and cross polarized enhanced backscattering from manufactured two-dimensional very rough surfaces at millimeter wave frequencies," *Radio Science*, Vol. 29, No. 5, 1275–1291, September-October, 1994.